How far can membrane characteristic parameters bestow at the membrane distillation performance: Modeling and simulation?

Salah S. Ibrahim and Qusay F. Alsalhy*

Chemical Engineering Department, University of Technology-Iraq, Alsinaa Street 52, Baghdad 10066, Iraq

Keywords: Membrane Distillation; VMD; Membrane parameters; Mathematical modeling; Desalination

---

Corresponding Author: Prof. Dr. Qusay F. Alsalhy, Email: qusay_alsalhy@yahoo.com, qusay.f.abdulhameed@uotechnology.edu.iq, Mobile: +964-7901730181.

Abstract

A mathematical model of simultaneous heat and mass transfer was presented to describe for the first time the effects of the variation in the characteristic parameters of the membrane during the VMD process on the permeation flux. The modelling approach was derived by dividing the module axially into multi-cells and a set of nonlinear simultaneous equations representing the VMD process were numerically solved via FSOLVE code. The validation of the presented model was estimated by simulation with a wide range of 135 diverse published experimental results related to the influence of various operating conditions, module properties, and membrane characteristics on the water permeation flux through the membrane. A good agreement was obtained between the experimental data and the results of the developed model. The same change in the membrane characteristics during the MD operation reported experimentally in the literature was confirmed by the simulation results of the developed model.

Introduction

As the global population continues to increase, the gap between the available and desired amount of clean, potable water is expanding, and it is approaching critical levels in some parts of the world [1]. Urbanization and industrialization continuously deplete fresh water sources. It is expected that by 2025, 60% of the world's population will suffer from unhealthy water, with water shortages in developing countries causing 90% of the disease burden. Therefore, it is necessary to find methods to supply affordable and healthy water [2].

Earth's seas and oceans comprise 96.5% of the Earth's water, with 0.8% considered to be fresh water, and the ice caps at 1.7%. One percent of the Earth's water is brackish or slightly salty water that exists as groundwater in salty aquifers and as surface water in estuaries as reported by United States Geological Survey [3]. Thus, in the past few decades, there has been increasing attention to desalination technology for use on saline water because of global demands for fresh water. A number of desalination technologies have been developed, with the most common being membrane and thermal processes. Salt concentration, economics, and the quality of water produced were the main reasons for the selection of a particular desalination process. Reverse osmosis (RO) and membrane distillation (MD) are valuable potential membrane processes for saline water desalination, with the goal of producing fresh water [4].

In the MD process, microporous and hydrophobic membranes are used and made mainly from hydrophobic polymers, such as polypropylene (PP), polytetrafluoroethylene (PTFE), and polyvinylidene fluoride (PVDF). The driving force in MD is the gradient of the solvent partial pressure through the wall of the membrane, which is related to the membrane's vapor pressure. In the desalination process by MD, the feed solution is heated to increase its vapor pressure, which produces a gradient between the partial pressure across the membrane. At the vapor-liquid interface of the membrane's pores, hot water is evaporated, so that only vapor can penetrate across the membrane. Various common configurations of MD may be employed, such as sweep gas membrane distillation (SGMD), air gap membrane distillation (AGMD), direct contact membrane distillation (DCMD), vacuum membrane distillation (VMD), vacuum assisted air gap membrane distillation (VA-AGMD), thermostatic sweeping gas membrane distillation (TSGMD), and liquid or water gap membrane distillation (LGMD/WGMD) [5-7]. The MD process has several benefits, including that it (1) can be operated at a temperature lower than the boiling point of the feed solution, (2) can be operated at low pressures, (3) enjoys a high separation performance of the nonvolatile solute, (4) has potential applications for producing distilled water, and (5) works with high osmotic pressure. These benefits make MD more valuable compared with other separation processes [5].

MD has been the subject of worldwide academic studies; however, from an industrial and commercial viewpoint, MD remains under evaluation, with various conflicting viewpoints regarding its advantages. Although today, it is not often employed by industry, the MD process is now being developed, especially for desalination testing [9].

VMD configuration had been proposed because for the same temperature gradient across the membrane and for similar affected variables, the permeate flux of VMD is usually

higher than that of other MD configurations. However, the difference between the pressure in the pores and the hydrodynamic pressure of the feed solution cannot exceed the liquid entry pressure (LEP), because the potential of wetting the membrane in VMD is often larger than in other common configurations of MD [10]. VMD arose as an effective area of research with water desalination applications in the 1990s. It is considered a highly thermally efficient process as it neglects the heat loss by conduction within the membrane wall because of low pressure (vacuum) at the membrane's permeate side and because the mass transfer resistance is decreased by deaeration (i.e., minimizing the molecular diffusion resistance) [9,11].

Many modelling attempts appear in the literature, with models for VMD [2, 9, 11-26]. In a comprehensive review of MD modeling, Lawson and Lloyd (1997) [27] reported that the main mathematical modelling differences found in the literature were focused on the mechanisms of heat and mass transfer through the membrane to evaluate the permeate flux.

In VMD, the heat transfer by conduction across the wall of the membrane was neglected by most researchers. It is also neglected in the present study due to the low pressure on the permeate face of the fiber [9, 18, 23, 26]. However, this conductive heat transfer was taken into account by other researchers [2, 19-22]. Also, the permeate side the thermal boundary layer was neglected in most research, but it was considered by some studies [2, 21]. In the present model, the thermal boundary layer was neglected because the heat transfer in the permeate face of the fiber was considered only by the vapor that exceeds the fiber wall toward the vacuum permeate zone.

Air (i.e., non-condensable gas) inside the pores is removed from the fiber during the VMD process due to the total pressure difference at the two sides of the fiber. Accordingly, the convective mass transfer in VMD occurs in contrast to other MD configurations, which have constant total pressure across the fiber sides and characterized by a diffusion of the migrated vapor through the entrapped air inside the pores of the fiber and without convective mass transfer through it. In addition, various mass transfer mechanisms across the membrane in the literature discussed mechanisms based on the Knudsen flow [12-14, 17, 24-26]. Other researchers have developed a model integrating the Knudsen-Poiseuille flow [11, 15, 16, 19], while still others have developed models using the transport mechanisms of molecular, Knudsen, and Poiseuille flows [18, 21, 22]. Other models of MD used an empirical correlation to predict the permeate flux through fitting (i.e., using multivariate regression problems) the experimental results based on the affected input parameters and using programming techniques such as an artificial neuron network (ANN). This type of model has been extensively applied in various fields of science, medicine, and technology and is not

dependent on explicit expressions of principles to govern equations that describe the mechanisms of the process. Instead, it is dependent on the process input-output complex relationship, often referred to as a "black-box" model. This approach usually gives good agreement between the predicted and experimental results [28] or with the experimental data extracted from the literature [29]. Hence, these models could be considered valid for simulations, when using a similar experimental rig. In their developed mathematical models of the VMD process, many studies investigated the influences of various parameters on the performance of the membrane, such as operating conditions and configurations of the module (i.e., countercurrent and cocurrent flow patterns, and the length and number of fibers). To the best of this researcher's knowledge, the changing effect of the membrane parameters during the MD operation was not been studied or described in the literature [2].

Therefore, in the present study, a mathematical VMD model was developed to evaluate the permeation flux of a shell-and-fibers VMD module used for water desalination. The effect of membrane characteristics (i.e., porosity, mean pore size, thickness and tortuosity), operating conditions, module design (i.e., packing density and the length of the hollow fiber) were considered in this mathematical modelling. In the present model, the fiber length was divided into similar consecutive cells and utilized a numerical reiterative method for solving the series of simultaneous nonlinear heat and mass transfer equations that control the desalination by the VMD process for each cell along the module. Most parameters that might affect the process were considered in this developed mathematical model, and their effects were studied extensively. The two-dimensional (2-D) model could predict the water permeation flux through the evaluation of the feed temperature and composition profiles at the bulk and membrane surface radially and axially based on the given input data of membrane characteristics and operating conditions. The model validity was evaluated by comparing its prediction widely with various experimental data summarized in the literature.

Theoretical Model

VMD is a complicated physical separation process in which both heat and mass transfer are involved simultaneously. In this process, the more volatile molecules will move within the pores of the hollow fiber from the warmer to the cooler side, that is, from the high pressure region in the feed side to the low pressure region in the permeate side, as depicted in Figure 1.

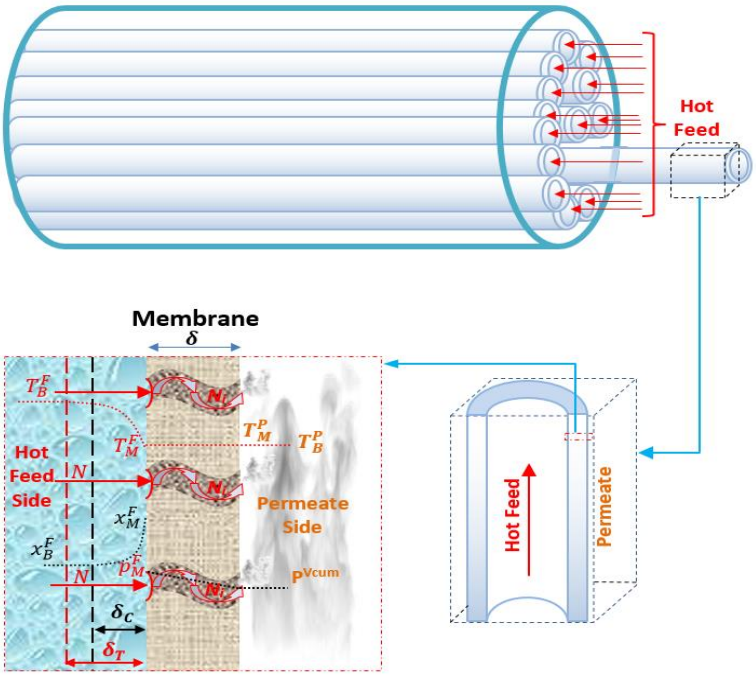

Figure 1. Hollow fiber membranes module with heat and mass transfer in VMD.

In general, the mechanism of water mass transport in the VMD process could be described as water evaporation at the hot hollow fiber feed side followed by water vapor movement within the pores of the hollow fiber toward the permeate side by the applied vacuum pressure. This transported vapor across the membrane is limited to the thickest and most tortuous path of the hollow fiber, which contributes significantly to the mass and heat transfer resistances. By selecting suitable hollow fiber material and the proper pressure gradient across the hollow fiber wall, condensation within the pores was prevented. The simultaneous heat and mass transfer that occurs in the VMD process results in a complex mechanism of heat transfer. As a result, the rate of mass transfer was affected by both the heat flux and the coefficients of the boundary layer heat transfer on the hot side. Therefore, the influence of temperature and concentration polarization was taken into consideration in the present model.

The pressure gradient between the partial water pressure (p_M^F) at the vapor-liquid interface on the hot fiber side and the permeate vacuum (P^{Vcum}) was the main driving force for the permeation of the water vapor within the pores of the hollow fiber, as depicted in Figure 1. Figure 1 show that the hot feed solution is considered to be a real solution using thermodynamic consideration by estimating the water activity coefficient. Because the conductive heat losses in the VMD process were neglected due to the low pressure at the permeate side, it was assumed that there was no temperature gradient across the fiber. Also, the thermal boundary layer at the permeate side was neglected due to the assumption of

constant temperature in the entire permeate evacuated chamber and perfect insulation for the module, where only the energy of the vapor penetrating the fiber wall was taken into account.

Below are other assumptions of the developed model:

- No hollow fiber wetting and no capillary condensation occurred inside the pores of the hollow fiber; thus, the retentate of the nonvolatile compounds in the feed was assumed to be 100%.
- The liquid and vapor phases were in thermodynamic equilibrium at the vapor-liquid interface at the surface of the fiber on the feed side.
- Along the path of the transported vapor within the fiber, the total pressure was considered as a variable parameter; therefore, a viscous (Poiseuille) flow mechanism was considered.
- The entrapped air in the pores was displaced by the vacuum applied at the permeate side; therefore, a single-gas convective mass transfer was considered across the fiber, and the resistance due to the molecular-molecular collision through the fiber pores was ignored (i.e., the ordinary molecular diffusion was neglected).
- A uniform pore size of the hollow fiber membrane was considered (e.g., the distribution of the pore size was ignored).

The analysis of heat and mass transfer was conducted by dividing the module into mini-modules, with each hollow fiber in the module divided into n elements, as depicted in Figure 2.

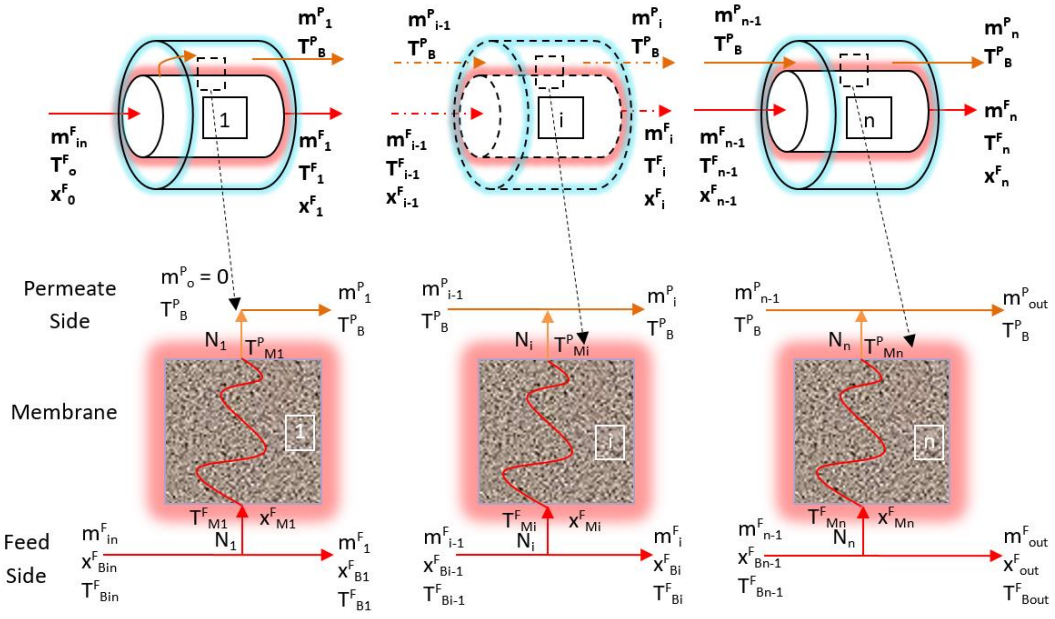

Figure 2. Schematic representation of the hollow fiber VMD cells.

The equations that control the boundary layer of the heat and mass transport were obtained for the steady state conditions, as shown in Figure 1. As depicted in Figure 2, the magnitude of heat and mass transported to and from the adjacent surface of the hollow fiber were dependent

upon the stream of the permeate vapor on the shell side and the stream of the feed on the lumen side. The heat and mass transport equations described below were applied depending upon the physical characteristics of the lumen (feed), shell (permeate), and hollow fiber membrane side for each unit, as depicted in cell *i*, as a typical unit in Figure 2:

Lumen side (feed side)

- **Heat transfer**

The basic principles of heat transfer and the theory of the thermal boundary layer imply that the fluid displayed its temperature profile only in this region. The thermal boundary layers throughout the VMD module appeared only on the feed side adjacent to and along the separated microporous membrane, as shown in Figure 1.

Heat transfer within the boundary layers adjacent to the hollow fiber at the side of the feed stream frequently limit the mass transfer because the heat rate related to the vapor-liquid interface is responsible for vaporizing the liquid that would penetrate the membrane. The phenomenological models are complicated for the MD process because of the microscopic mechanism at the hollow fiber surface. Therefore, the temperature of the feed stream or the precise temperature at the membrane surface is an essential factor affecting the permeate flux; it is complicated to estimate this temperature using the basic principle of heat transfer alone [2]. The net heat transported within the boundary layer of the feed side of the *ith* cell of the inner membrane surface is depicted in Figure 2. Thus, Eq. 1 can be expressed as follow:

$$Q_i^F = h_i^F A_{ri}(\bar{T}_{Bi}^F - T_{Mi}^F) \quad (1)$$

where h_i^F is the heat transfer coefficient, $\bar{T}_{Bi}^F$ is the average bulk temperature, and T_{Mi}^F is the fiber surface at the feed side. To evaluate h_i^F, several Nusselt number empirical correlations for laminar and turbulent flows have been reported [6, 30-32]. On the fiber lumen side, Eqs. 1a and b may give suitable predictions for the present model of the heat transfer coefficients for the laminar and turbulent flows, respectively [9, 32].

$$Nu = 1.86\left(\frac{Re\ Pr}{L/D}\right)^{1/3}\left(\frac{\mu}{\mu_w}\right)^{0.14} \quad \text{if } G_z \geq 100 \quad (1a)$$

$$Nu = \left(3.66 + \frac{0.0668\ G_z}{1+0.04(G_z)^{2/3}}\right)\left(\frac{\mu}{\mu_w}\right)^{0.14} \quad \text{if } G_z < 100 \quad (1b)$$

$$G_z = Re\ \mathrm{Pr}\frac{D}{L} \quad (1c)$$

$$\bar{T}_i^F = \frac{T_i^F + T_{i-1}^F}{2} \quad (1d)$$

$$A_{ri} = 2\pi r_i l \quad (1e)$$

where l is the element length, equal to the length of the fiber per the number of assumed elements.

The energy balance of cell *i* at the feed side (see Figure 2) was based on the change in the sensible heat between the inlet and outlet streams of the feed solution and the latent heat of the vaporization of the water that migrated through the side of the hollow fiber:

$$Q_i^F = m_{i-1}^F H_{i-1}^L - m_i^F H_i^L - N_i A_{ro} \Delta H_{Mi}^F \quad (2)$$

where N_i (kg/m^2 h) is the water mass permeate flux; A_{ro} (m^2) is the surface area based on the outer diameter of the hollow fiber; H^L and ΔH are the liquid water enthalpy and the enthalpy of the water vaporization, estimated by Eqs. 2a and b, respectively [32, 11], both in kJ/kg; and T is the temperature in K, as follows:

$$H^L = -1117.8 + 4.0312T + 2.0 \times 10^{-4} T^2 \quad (2a)$$

$$\Delta H = 3177800 - 2464.4T \quad (2b)$$

- **Mass transfer**

In the desalination process using the VMD technique, the mass transfer was carried out in two steps. The first was the liquid water transported through the concentration boundary layer near the fiber surface of the feed side (see Figure 1), where the composition of the salt compound increased from the bulk feed x_B^F to the surface of the fiber x_M^F due to the mass transfer resistance present across this layer (i.e., concentration polarization). The second step was the transportation of the water vapor across the hydrophobic microporous membrane, which occurred by various mechanisms.

The transportation of the liquid water within the concentration boundary layer of the feed side formed a high salt concentration region at the surface of the hollow fiber because of the movement of water vapor molecules across the fiber wall, creating a higher salt concentration at the fiber surface than in the bulk feed. Over time, the resistance imposed by this layer became considerable against the movement of the water vapor molecules, leading to a salt concentration at the fiber surface on the feed side, where the water mass flux also declined. Unfortunately, at the fiber surface, the concentration of the salt could not be estimated experimentally. The high concentration polarization coefficient (CPC), which is the ratio of the salt concentration at the fiber surface on the feed side (C_M^F or x_M^F) to the bulk feed concentration, (C_B^F or x_B^F) caused the permeation flux to decrease. However, the CPC can only be theoretically determined throughout the MD modeling approach [19].

According to the theory of mass transfer, in the concentration boundary layer, the mass flux of liquid water can be calculated using Eq. 3 [33]:

$$N_i = k_i^F C_T M w t_w \ln\left(\frac{x_{Mi}^F}{x_{Bi}^F}\right) \quad (3)$$

$$\bar{x}_{Bi}^{F} = \frac{x_{Bi}^{F} + x_{Bi-1}^{F}}{2} \quad (3a)$$

where N_i (kg/m^2 h) is the water permeate mass flux, C_T (kmol/m^3) is the total feed bulk concentration, x^F is the feed salt mole fraction, and k_i^F(m/h) is the mass transfer coefficient. From the principles of heat and mass transfer, the mass transfer coefficient was calculated using the empirical correlations of the heat transfer after substituting the Schmidt number ($\mu/\rho.D_{AB}$) for the Prandtl number and the Sherwood number ($k.D/D_{AB}$) for the Nusselt number. In general, this assumption is accepted because of the similarity of the two transport processes that take place using identical geometries [34].

As long as membrane wetting can be avoided, the most attractive property of the MD process is that salt or any nonvolatile component can be totally rejected by the membrane. Theoretically, this assumption was often used in the modelling literature because it is very close to the actual state, where more than 99% salt rejection is often obtained. Thus, on the feed side, a salt mass balance yields Eq. 4:

$$x_i^F = \frac{m_{i-1}^F}{m_i^F} \frac{(Mwt_{sol})_i}{(Mwt_{sol})_{i-1}} x_{i-1}^F \quad (4)$$

where, salt material balance on cell i on the feed side (see Figure 2) can be based on one of two cases:

(a) salt weight fraction w_i^F: $m_i^F w_i^F = m_{i-1}^F w_{i-1}^F$ (٤a)

(b) salt mole fraction x_i^F: $\frac{m_i^F}{(Mwt_{sol})_i} x_i^F = \frac{m_{i-1}^F}{(Mwt_{sol})_{i-1}} x_{i-1}^F$ (4b)

In much of the literature on mass fraction (or weight percent) for the expression of the feed salt concentration, the weight fraction w_i to mole fraction x_i conversion was expressed as follows:

$x_i = \frac{w_i}{Mwt_i}(Mwt_{sol})$, where $Mwt_{sol} = \frac{1}{\sum w_i/Mwt_i}$ (4c)

And the mole fraction x_i to weight fraction w_i conversion is

$w_i = \frac{x_i(Mwt_i)}{Mwt_{sol}}$, where $Mwt_{sol} = \sum x_i(Mwt_i)$ (4d)

On the feed side, the total mass balance is expressed as follows (see Figure 2):

$$m_i^F = m_{i-1}^F - N_i A_{ro} \quad (5)$$

Two moles of ions are liberated by dissolving each mole of NaCl. When dissolving this salt in water, the framework of sodium chloride disbands as the Cl^- and Na^+ ions become enclitic by the polar molecules of water. Therefore, the dissociation of sodium chloride in water can be written as follows:

$$NaCl_{(s)} \xrightarrow{H_2O} Na^+_{(aq)} + Cl^-_{(aq)} \quad (6)$$

So, the mole fraction of water in solution x_w is calculated by $x_w = 1 - 2x$, where, $x \equiv x_{NaCl}$ is the NaCl mole fraction in solution [35, 36].

Shell side (permeate side)

- **Heat transfer**

The energy transport on the permeate side (outer surface) is the same as that transferred by the vapor mass transfer through the membrane (see Figure 2):

$$Q_i^P = N_i A_{ro} \Delta H_i \quad (٧)$$

where ΔH_i is the latent heat of vaporization, estimated by Eq. 2b.

- **Mass transfer**

Based on the assumption of 100% salt rejection by the hollow fiber, only the water vapor will be transported to the permeate side. Therefore, no concentration boundary layer was formed at the permeate side of the fiber. On the permeate side, the total mass balance becomes (see Figure 2):

$$m_i^P = m_{i-1}^P + N_i A_{ro} \quad (8)$$

where there is no mass flow rate entering the first cell of the fibers [i.e., for cell i = 1 $m_o^P = 0$, see Figure 2]. The permeate mass flow rate will be established beyond cell i.

Membrane side

- **Heat transfer**

In VMD, the heat transfer by conduction within the body of the fiber is ignored due to the low pressure on the fiber permeate side [9, 24, 27]. Therefore, the heat transferred within the fiber results from the vapor flowing through it:

$$Q_i^M = N_i A_{ro} \Delta H_i \quad (9)$$

At steady state

$$Q^F = Q^M = Q^P \quad (10)$$

- **Mass transfer**

In VMD and other MD processes, the mass transfer within the hollow fiber wall is normally described by assuming a linear relationship between the vapor partial pressure gradient across the fiber and the mass flux (N) by the membrane distillation coefficient (MDC) (K_i^M) [9, 24, 27].

Thus, $N_i = K_i^M (p_{Mwi}^F - P^{Vcum})$ (11)

where P^{Vcum} is the vacuum pressure at the permeate side (see Figure 1); and p_{Mwi}^F is the partial water pressure, evaluated at the conditions of the feed fiber surface, depending on the assumption of the vapor-liquid thermodynamic equilibrium at the vapor-liquid interface:

$$p_{Mi}^{F} = (1 - 2x_{Mi}^{F})\alpha_i P^{VF} \quad (11a)$$

where α_i is the water activity coefficient in the aqueous solution of sodium chloride, calculated by [9, 11, 27, 37]:

$$\alpha_i = 1 - 0.5x_{Mi}^{F} - 10(x_{Mi}^{F})^2 \quad (11b)$$

and P^{VF} is the water vapor pressure at the fiber surface of the feed side (vapor-liquid interface), calculated by the Antoine equation at the temperatures of T_{Mi}^{F}, for the feed and permeate, as follows:

$$P^{V} = exp\left(23.1964 - \frac{3816.44}{T-46.13}\right) \quad (11c)$$

where P^{V} is the vapor pressure of the water (Pa), and T is the temperature (K) [11].

As listed previously, various mechanisms have been proposed for the migration of vapor within the porous hollow fiber because in the VMD process, the molecular diffusion is not sufficient as the hollow fiber is assumed to be evacuated from the air. Consequently, only the Knudsen and viscous flow diffusion have been considered in the present model. The mass transfer mechanisms depend on the Knudsen number (Kn), which is defined as the ratio of the mean free path (λ) of the migrated molecules to the fiber pore size: i.e., Kn = λ/d. For water vapor molecules, the following equation can be used to calculate the mean free path (λ) [11]:

$$\lambda = \frac{k_B \bar{T}}{\sqrt{2}\pi P_T \sigma_W^2} \quad (12)$$

where k_B is defined as the Boltzmann constant (1.381×10^{-23} J K^{-1}), σ_W is defined as the collision diameter for the water vapor (2.641×10^{-10} m), and P_T is defined as the total absolute pressure (Pa). At a vacuum pressure of about 1000 Pa, with temperatures ranging from 30-80°C the water mean free path in air ranged from 3.5-3.65 μm [20], which was larger than the diameter of the pore on the fiber (0.1-1 μm) that is often used for the MD process. Thus, the integration of the Knudsen diffusion and the viscous flow of the vapor transfer mechanism within the fiber pores almost controls the mass transfer in VMD [6]. Because of the inverse proportion between the mean free path and the total absolute pressure (see Eq. 12), the mean free path of the molecules transferred within the pores of the fiber were higher in VMD than in other MD configurations. Therefore, different mechanisms of the mass transfer can be used when a similar fiber is utilized for various MD configurations under different operating conditions. Khayet and Matsuura (2011) [6] state that in all the reported theoretical VMD studies, they assumed that the membranes were uniform and consisted of non-interconnected cylindrical pores. When the pore size (d) is less than 0.1 λ and Kn is higher than 10, the collisions between the molecules and the wall of the fiber pore occur more often than the collisions between the molecules themselves. Therefore, the Knudsen diffusion is the

dominant mechanism that depicts the migration of the water vapor within the pores of the fiber. When 0.1 λ < d < 100 λ and Kn ranges between 0.01 and 10, the transition flow dominates, and the combined Knudsen/viscous mechanism models water vapor transportation across the membrane. In contrast, if Kn < 0.01 (i.e., d > 100 λ), viscous flow is utilized to depict the mass transfer within the membrane.

In the present model of the VMD process, all the mass transfer mechanisms of water vapor within the fiber were considered according to the above limitations, and a uniform pore size was assumed for the entire membrane, so the net microbial desalination cell MDC K_i^M of VMD can be expressed as follows:

$$K_i^M = \begin{cases} \beta_i^K & \text{Kn} < 0.01 \\ \beta_i^V & \text{Kn} > 1.00 \\ \beta_i^{K-V} & 0.01 < \text{Kn} < 1.00 \end{cases} \quad (13)$$

$$\beta_i^K = \frac{4}{3}\sqrt{\frac{2}{\pi}}\frac{r\epsilon}{\tau\delta}\left(\frac{Mwt_w}{R\bar{T}}\right)^{1/2} \quad (13a)$$

$$\beta_i^V = \frac{1}{8}\frac{r^2\epsilon}{\tau\delta}\frac{\bar{P}}{\mu RT} \quad (13b)$$

$$\beta_i^{K-V} = \left[\beta_i^K + \beta_i^V\right] \quad (13c)$$

where ϵ, τ, r, and δ are the void fraction porosity, tortuosity, radius of the pore, and hydrophobic fiber thickness, respectively; R is the gas constant; and T is the absolute temperature; $\bar{P}$ is the mean pressure in the pores; and $\bar{P} = (p_M^F + P^{vacm})/2$.

Mathematical model

One of the main purposes of mathematical modeling is to predict the permeate flux based on the operating conditions, module design, and membrane characteristics. Extensive knowledge about the heat and mass transport mechanisms in the VMD configuration led to understanding the process and building a proper mathematical model for appropriate predictions and process simulations to work as an infrastructure for industrial design. Implicitly, the model solves equations numerically that have described the heat and mass transfers in the VMD process and also adapts its performance according to output results based on the input data.

In the present mathematical model based on the VMD process input parameters (IPs), [i.e., feed temperature, concentration, flow rate, membrane characteristics, and module parameters], a number of unknown variables could be calculated to evaluate the model's performance. These unknowns are the model output parameters (OPs), which were mainly the permeate flux, temperature, concentration, and flow rate of the outlet feed, plus the surface fiber temperature, concentration at the feed side, and the rate of heat transfer.

Thus, the present model had the ability to solve the set of nonlinear equations produced from the heat and mass balances on each cell of a series of multicells (see Figure 2) via a suitable numerical solution. The input parameters (IPs) of cell 1 were used by the model to evaluate the output parameters (OPs) of this cell, which were used as IPs for the next cell (i.e., cell 2), etc. The present developed mathematical model was based on programming written by MATLAB® code to solve these equations of the two-dimensional cylindrical geometry of hollow fiber. The system consists of seven nonlinear simultaneous equations (i.e., Eqs. 1, 2, 3, 4, 5, 7, and 11) that would be solved simultaneously to estimate the seven stated OPs by using the FSOLVE code, which is a built-in subroutine in MATLAB® for solving a system of nonlinear simultaneous equations using the least square method. The solution's elapsed time depends significantly on the number of cells assumed, and n = 10 was an appropriate number for all experimental data. The elapsed time was less about 10-15 seconds for each run (point result) using a PC with an Intel® Core™ i7-8750 H CPU processor @ 2.20GHz 2.21GHz and installed memory (RAM) of 16.0 GB (15.8 GB usable).

Results and Discussion

Membrane characteristics

Eq. 11 governs the prediction of vapor mass flux across the membrane used in the VMD process. This equation relates two key parameters: (1) the driving force (pressure gradient across the fiber wall), and (2) the resistance (reciprocal of the membrane distillation coefficient [1/MDC or $1/K_i^M$]). Based on Eqs. 11 and 11a-c, the driving force depends on the vapor pressure, salt concentration, and water activity coefficient as well as the degree of vacuum at the permeate side (a constant), whereas the former variables could be determined theoretically and were considered for each cell along the module during the operation. The resistance ($1/K_i^M$) depends greatly on the membrane characteristics, as shown by Eqs. 13a and b, where the resistance is directly proportional to the mean pore radius (r) and porosity (ε) but inversely proportional to the thickness of the fiber (δ) and tortuosity (τ). Accordingly, Lawson and Lloyd (1997) [27] reported the dependence of the permeation flux (N) on the membrane characteristics, which can be expressed as $N \propto \frac{r^{\sigma}\epsilon}{\delta\tau}$, where σ = 1 or 2 for the Knudsen diffusion and viscous fluxes, respectively. Therefore, theoretically, the fiber characteristics play a very important role in evaluating the optimal permeation flux. However, in the MD process, there is always a significant effect of the membrane characteristics that were assumed not varied during the operation in changing the operating conditions (mainly temperature and pressure). Also, across the membrane, several mechanisms of mass transfer

may occur simultaneously because of the distribution of the pore sizes at the surface of the membrane. However, the pore size of the entire fiber is assumed to be uniform in most theoretical studies, although it depends on the operating conditions (e.g., temperature and pressure) as do other membrane characteristics that are often assumed to be constant during the MD operation in modelling studies. The organic membranes used in most MD processes are polymeric materials (polymeric porous media), and membrane length and thickness cannot be considered a constant value with changes in the temperature and pressure due to membrane expansion and compression with increasing temperature and pressure, respectively [38, 39]. Also, the movement of the more volatile molecules across the fiber wall takes tortuous paths, which leads to flux decay due to the extra mass transfer resistance of the added lengths inherent in tortuous paths. Due to the higher predicted values of the permeation flux across the membrane when compared with the corresponding experimental data, most mathematical models consider the tortuous path to be a significant factor that must be adjusted for an appropriate prediction of the permeate flux. Therefore, the mass transfer resistance within the fiber not only depended on the thickness of the fiber (δ) but precisely depended on the tortuous path (δτ) for more volatile molecules to exceed the boundaries of the membrane. Thus, the main reason for tortuosity (τ) to be taken into account in mass transfer correlations (e.g., Eqs. 13a and b) was to correct for and improve the theoretical predictions of the permeate flux. The value of the tortuosity was assessed in different ways in the literature, of which a value of 2 was frequently assumed for the tortuosity of the fiber to predict the transmembrane flux [6]. The value of the tortuosity can also be calculated using various correlations of the tortuosity related with the porosity, such as by using the two well-known equations $\tau = 1/\epsilon$ or $\tau = (2-\epsilon)^2/\epsilon$ [40]. However, other studies used assumed values of tortuosity to make the simulation results fit more closely with the experimental results and were often beyond the range of these two well-known equations, as shown in Table 1.

Table 1: Tortuosity values were used in literature

Membrane type	Porosity %	$\tau = 1/\epsilon$	$\tau = (2-\epsilon)^2/\epsilon$	τ used in reference	Ref.
PTFE	66.8	1.497	2.656	4.2	[41]
	72.6	1.378	2.236	6.6	
	72.8	1.374	2.223	10.1	

The tortuosity and other membrane characteristics are significant parameters limiting the permeate vapor flux, but no systematic experimental study has been conducted to measure these membrane characteristics in the MD process under various operating conditions because

the membrane's inner structure is complex. Thus, assuming uniform values for the membrane characteristics during the MD operation may lead to inaccurate predictions of the model.

However, Zhang et. al. (2013b) [42] investigated the impact of operating conditions on the characteristics of the fiber, such as the compressibility effect on the hollow fibers used in the VMD process. They indicated that the hollow fibers were compressed under the pressure difference at the two membrane sides (e.g., between 100 and 180 kPa, depending on the velocity of the feed stream). Zhang et. al. (2011, 2012) [38, 39] also found that the compression of the membranes led to changes in the membrane characteristics (i.e., reduced porosity, pore size, and membrane thickness). All of these characteristics had a direct effect on the mass transfer of water vapor within the fiber, as seen in Eq. 13. Figure 3 shows the theoretical impact of hollow fiber characteristics (i.e., porosity, pore size, and membrane tortuosity) on the permeate flux, based on [42]. More details are given in Table 2 for Zhang's membrane A, which was used in the VMD process for modules with packing densities of 48% and 32%. As displayed in Figure 3, there was a significant effect of these fiber characteristics on the permeate flux.

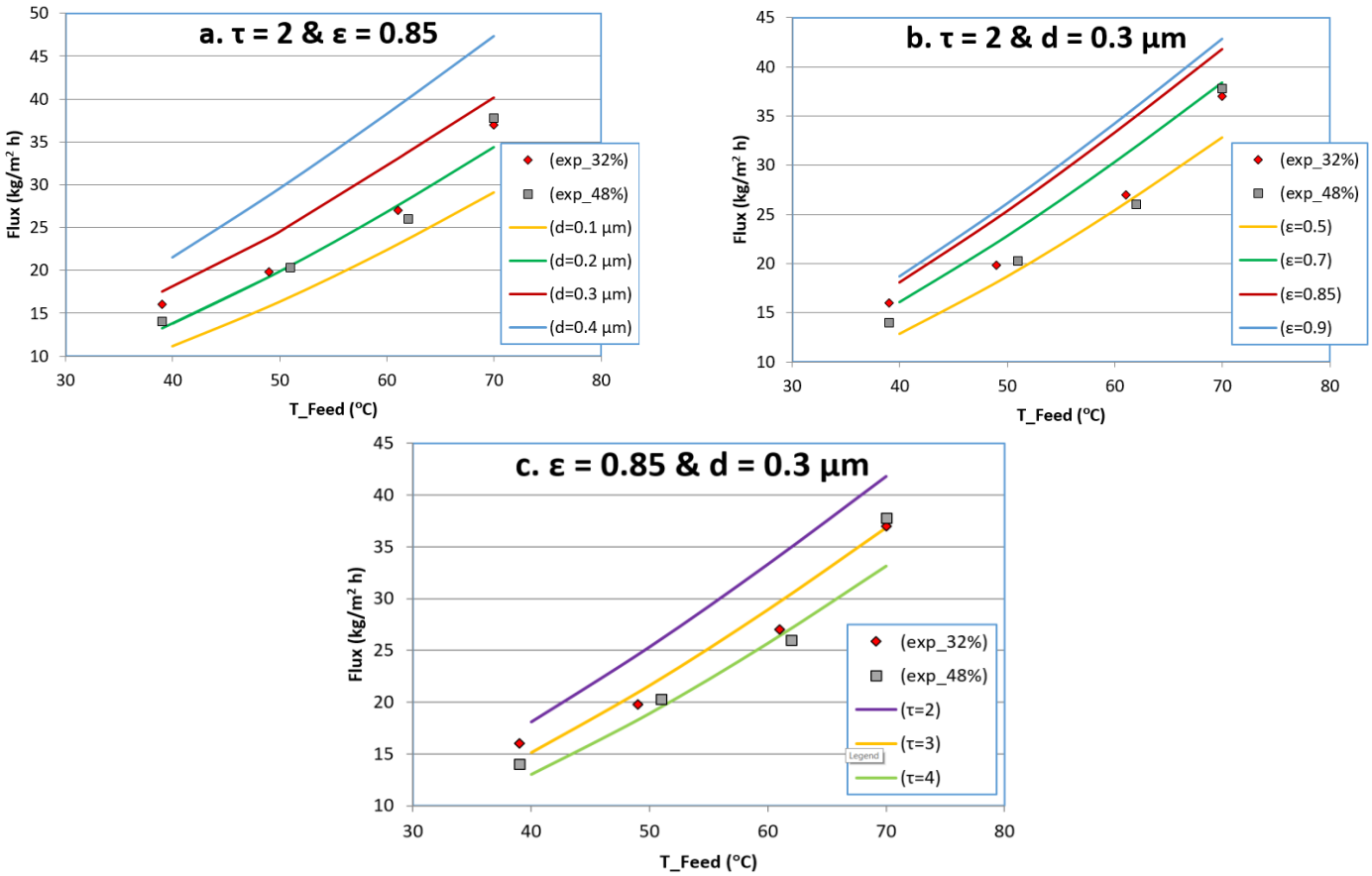

Figure 3. Effect of feed inlet temperature and membrane characteristics on permeate flux experimentally [Zhang, et. al., (2013b)] and theoretically. [u_F = 0.81 m/s, P^{vacm} = 3 kPa_abs and salinity = 120 µS/cm].

In Figure 3a, the predicted flux increased by 92% at 40°C but only 63% at 70°C, when the change in the pore size was assumed to be between 0.1 and 0.4 µm. These simulation results were estimated based on a membrane porosity of 0.85, as given in Table 2, with an assumed tortuosity of 2. Figure 3a clearly illustrates agreement between the experimental data and predicted results, with a reduction in the fiber pore size differed than is listed in Table 2, where with an increase in the feed solution temperature, the solution vapor pressure also increased, causing an increase in the pressure difference at the membrane's sides. Zhang et. al. (2013b) [42] revealed that the reduction in the porosity and pore size of the fiber was due to the effect of membrane compressibility, which was identical to the results obtained by the current developed model.

Table 2: Summary of the specifications of membranes and operating conditions and of the hollow fiber modules used via VMD processes

Membrane type	**Fluorine containing material**			**Membrane A Fluorine containing material**			**Membrane B Fluorine containing material**		
Membrane code	32%	40%	48%	32%	40%	48%	L_1	L_2	L_3
OD (mm)	1.6	1.6	1.6	1.5	1.5	1.5	1.4	1.4	1.4
ID (mm)	0.8	0.8	0.8	0.8	0.8	0.8	0.7	0.7	0.7
Wall thickness (mm)	0.4	0.4	0.4	0.35	0.35	0.35	0.35	0.35	0.35
Shell diam. (cm)	2.5			2.5			2.5		
Length (cm)	25			25			15	25	35
Pore size (µm)	0.3			0.3			0.3		
Porosity (%)	85			85			85		
Number of fibers	63	80	97	63	80	97	80		
Inlet feed temperature (˚C)	40 – 70			40 – 70			40 – 70	60	40 – 70
Salt Concentration (g/l)	Tap water [120 µS/cm]			Tap water [120 µS/cm]			Tap water [120 µS/cm]		
Feed flow rate	0.4 – 2.56 (m/s)			0.4–2.56 (m/s)	0.4–2.1 (m/s)	0.4–2.1 (m/s)	0.56–2.78 (m/s)	1.15 (m/s)	0.56–2.78 (m/s)
Vacuum pressure (kPa_abs)	2 – 5			3.0			3.5 – 30		
Permeate flux data points	10	10	10	9	9	9	9	4	9
Total data points	30			27			22		
Reference	[19]			[42]					

Table 2 Continued

Membrane type	PTFE			
Membrane code	P-120	P-160	P-180	P-220
OD (mm)	2.5	2.5	2.5	2.4
ID (mm)	0.9	0.9	0.9	0.9
Wall thickness (mm)	0.8	0.8	0.8	0.75
Shell diam. (cm)	2.5			
Length (cm)	39			
Pore size (µm)	0.082	0. 12	0.22	0.46
Maximum pore size (µm)	0.3	0.38	0.52	0.75
Porosity (%)	26.2	35.9	42.8	63.4
Number of fibers	40			
Inlet feed temperature (˚C)	60 – 80			
Salt Concentration (g/l)	10 – 100			
Feed flow rate	40 (l/h)			
Vacuum pressure (kPa_abs)	6.325 – 21.325			
Permeate flux data points	14	14	14	14
Total data points	56			
Reference	[44]			

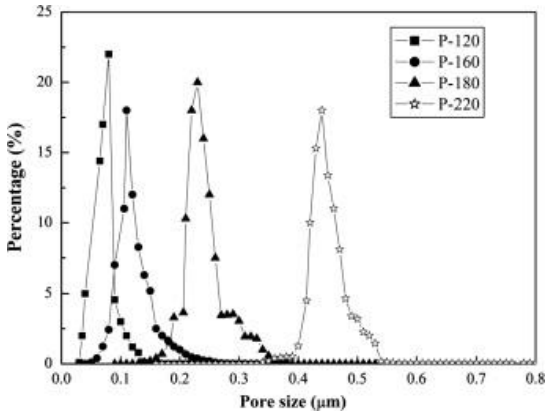

In Figure 3b, the predicted flux increased by about 46% at 40°C, but only 31% at 70°C, when the change in the porosity was assumed to be between 0.5-0.9, with the following fiber characteristics: pore diameter of 0.3 µm and assumed tortuosity of 2. Figure 3b shows that the permeate flux predicted by this model was consistent with the experimental data when the porosity was reduced due to the increasing vapor pressure of the feed solution. This reduction in the fiber porosity might be due to the effect of membrane compressibility because the model's results agree well with the experimental results of [42] in terms of the membrane compressibility effect on the fiber porosity. Figure 3c displays the given pore size and porosity listed in Table 2, with various assumed values of tortuosity from 2-4 and the predicted flux reduced from 28 to 21% at a temperature range from 40-70ºC, respectively. Figure 3c shows that the simulation results were more consistent with the experimental data with an increase in the tortuous path of the membrane. Figure 3 also shows that there is no particular value of the membrane characteristics that could be used to estimate the fitting permeation flux with temperature shifts because the temperature affects the feed vapor pressure. Consequently, the temperature affects all membrane characteristics, which impacts the permeate flux. Thus, more accurate values of these characteristics with shifts in temperature are required to accurately estimate the values of the permeation flux. Both the values of the membrane characteristics that were supplied by the manufacturer and those found by testing the membrane have a level of uncertainty [43]. Thus, due to the available

data of the membrane characteristics in the literature, the tortuosity was selected to be the adjustable parameter related to the mass transport resistance for vapor to penetrate through the fiber in the present model, which in turn can be used to discover the best prediction of the permeate flux in comparison with the experimental data.

Effect of feed temperature

The temperature of the feed represents one of the most significant practical operating parameters that drives the general MD process to maximize the permeate flux of more volatile compounds. The temperature of the feed is directly related to the main driving force of the permeate flux due to an exponential increase in the vapor pressure according to the Antoine equation (Eq. 11c) as the feed temperature increases.

The experimental effect of the inlet feed temperature on the permeate flux was obtained from [44], and the theoretical predicted flux by the present model are shown in Figure 4. The membranes were prepared polytetrafluoroethylene (PTFE) hydrophobic hollow fibers manufactured using a cold processing technique, including paste sintering, extrusion, and stretching. Four PTFE fibers were fabricated (i.e., P-120, P-160, P-180, and P-220), corresponding to the four stretching ratios of 120, 160, 180, and 220%, respectively.

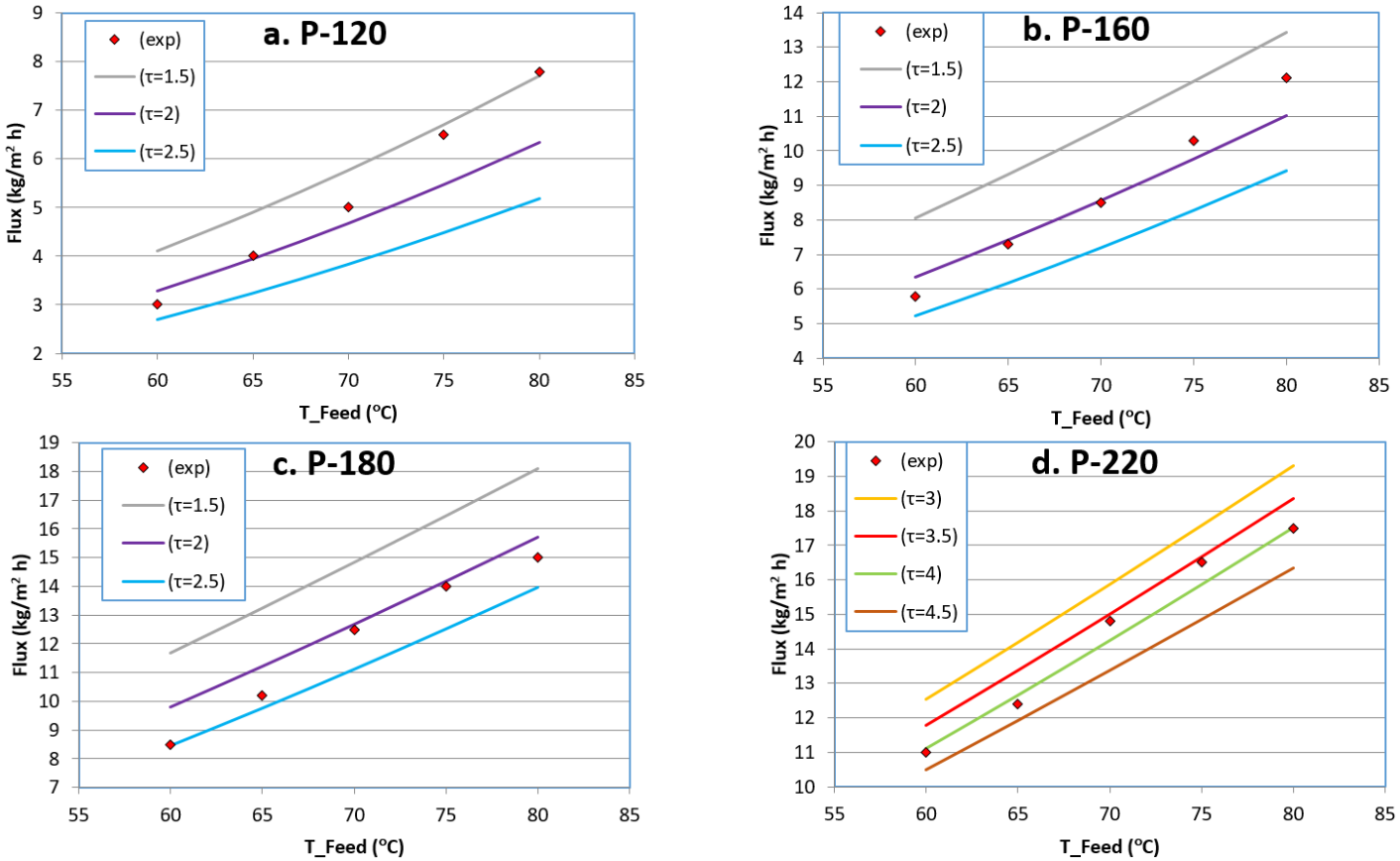

Figure 4. Effect of inlet feed temperature on permeate flux experimentally [44] and theoretically. [Q_F = 40 l/h, P^{vacm} = 6.325 kPa_abs and salt concentration = 3 wt%].

These fibers had various mean pore sizes and porosities, as summarized in Table 2. The increase in feed temperature directly affects the increase in the solution vapor pressure, which increases the compression effect on the membrane. Increasing the temperature of polymeric pores material of the fibers used in the VMD process results in expanding the lengths and thicknesses of the fibers, which expands the pore sizes and alters the mean pore size. Thus, as the feed temperature increases, there is competition between the effect of the solution vapor pressure and the membrane expansion on the membrane characteristics, as shown in Figure 4. The experimental data indicated that at T = 70°C, the permeation flux did not increase exponentially for all membranes.

The change in the tortuosity values reflects the change in the mass transfer resistance of the transported vapor molecules within the fiber thickness at various temperatures, according to the mass transfer principles used to predict the permeate flux theoretically. However, the decrease in the mass transfer resistance may also result from an increase in the fiber pore size and porosity with rising temperature. The optimal adequate predicted permeate flux could be obtained with respect to the experimental data by selecting a suitable value for the tortuosity. Figure 4 shows that the experimental water permeate flux rose with increases in the stretching ratios because of the increase in the mean pore size and porosity (see Table 2) as a result of their direct proportionality in the MDC; however, the simulation results were conducted to increase the tortuosity as the stretching ratios also increased. Zhu et al. (2013) [44] reported that from the pore size distribution results (Figure embedded in Table 2) the percentage of the mean pore size of all the fabricated fibers was about 20 ± 2%, while the rest (i.e., 80%) had pore sizes larger or smaller than the mean pore size of each fiber. As shown in Table 2, the maximum pore size of the fibers was larger than their mean pore size by various percentages, such as 266%, 217%, 136%, and 63% for P-120, P-160, P-180, and P-220, respectively. This could indicate that there was a greater degree of influence of a larger pore size than of the mean pore size on the permeation flux (e.g., P-120 > P-160 > P-180 > P-220). Also the pore size distribution (Figure embedded in Table 2) indicated that the percentages of the larger pore sizes than the mean pore size were higher than the percentages of smaller one. As a result, the required theoretical mass transfer resistances for fitting the predicted permeation flux (according to the required value of the tortuosity) were also increased, as follows: P-120 > P-160 > P-180 > P-220, as shown in Figure 4. This can be explained by the uniform pore size and porosity of each fiber used in the present simulation, which is expected to change based on the operating conditions.

Figure 5 displays experimental data from [19] on the influence of the inlet feed temperature on the permeate flux along with the flux predicted by the developed model. Zhang et al. (2013a) [19] tested comparable fiber characteristics in three similar modules with various packing densities, as summarized in Table 2. They found that there is no effect of the number of fibers inside the module on the water permeates flux, and the effect of the number of fibers on the total production of each module with time. Moreover, Zhang et al. (2013a) [19] stated that the experimental results of the permeate flux of the VMD process was not affected by the module's packing density. However, in Figure 5d, a few differences were observed among the experimental data of these modules under the same conditions. As reported by [19], this is because of the variation in the experimental vacuum pressure, where during the experiments there was an increment of change in the absolute pressure at the permeate side (shell side) at high temperatures (i.e., for modules with packing densities of 48%, 40%, and 32% as the temperature increased from 40 to 70°C, the increment of change in the absolute pressure changed from 2.1 to 5.7, 2.1 to 4.8, and 1.3 to 3.1 kPa, respectively). Thus, the average permeate pressures used in the present simulation were 3.9, 3.45, and 2.2 kPa for 48%, 40%, and 32% packing densities, respectively, as shown in Figures 5a-c.

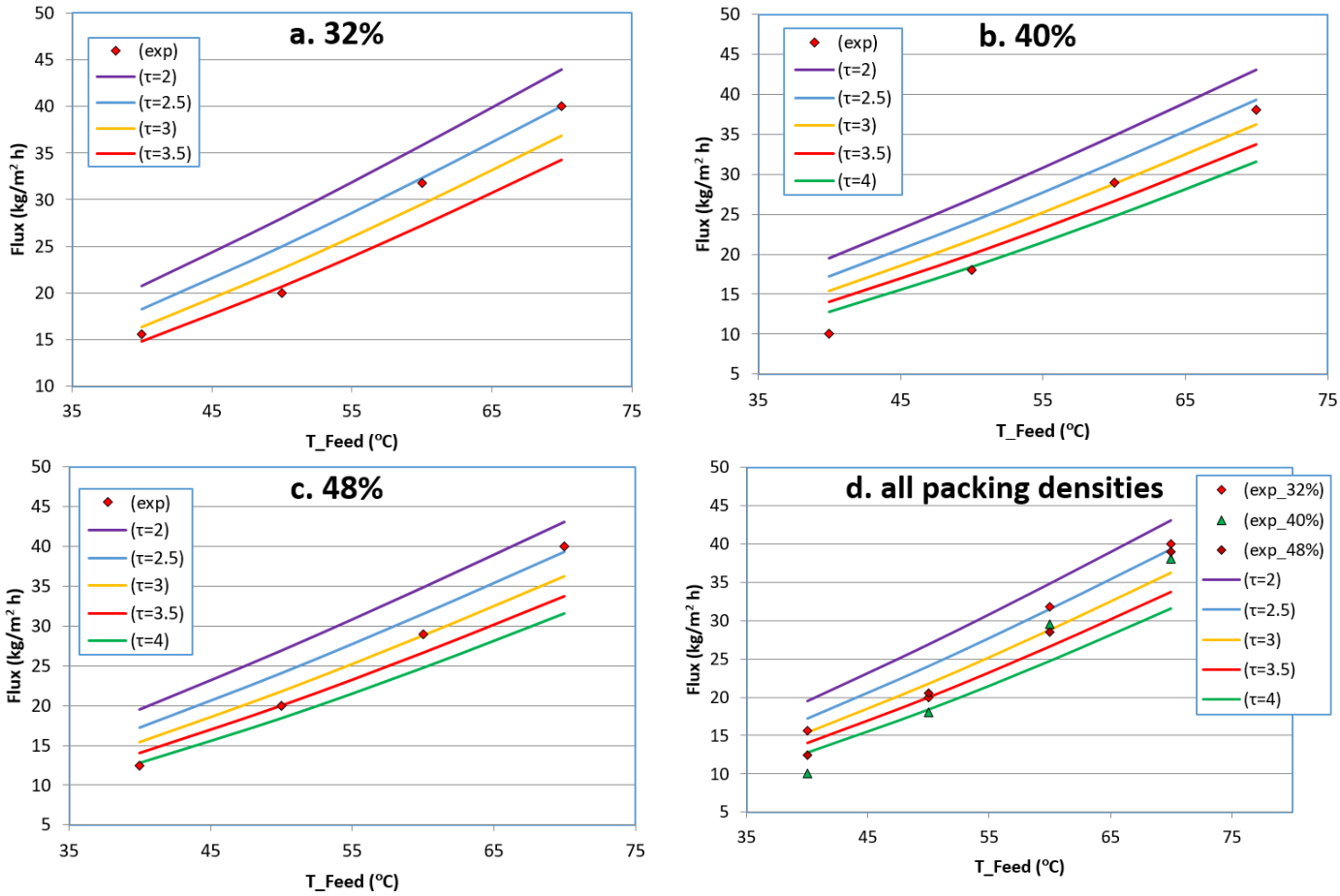

Figure 5. Effect of inlet feed temperature on permeate flux experimentally [19] and theoretically. [u_F = 0.8 m/s, P^{vacm} = 2.1 – 5.7 kPa_abs and salinity = 120 µS/cm]

Generally, the change in the permeate (vacuum) pressure had a significant effect on the VMD permeate flux. However, in Figures 5 a-c, the effective change range of the permeate pressure was not large and had little effect on the experimental and predicted flux. For example, when the pressure at the permeate side increased from 2 to 5 kPa, the predicted permeate flux increased by about 13% at 40°C and about 4% at 70°C. So, at the average pressure of 3.5 kPa used for all modules (see Figure 5d), the fitting tortuosity tended to decrease at a higher temperature (i.e., increased MDC). Also, there was no single value of tortuosity that could express the mass transfer resistance of the transported vapor through the fiber thickness at various temperatures. This observation may confirm the previous indication (see Figure 4) in the present study of the expected effect of the temperature on the solution vapor pressure, and thereby, on the porosity and pore size.

The temperature effect of the inlet feed on the experimental permeate flux was obtained from [42], with the effect predicted by the present model shown in Figure 6. Zhang et al. (2013b) [42] studied the effect of the hollow fiber packing density, feed velocity, module length, feed temperature, vacuum pressure, and membrane compressibility on the VMD performance. They used six modules of different membranes, lengths, and packing densities, with membranes labeled A and B, as described in Table 2. As shown in Figure 6a, there was some similarity in the experimental and theoretical results between the data of membrane A in Figures 6a and 5d due to some similarity between these two systems. In Figures 6b and c, where membrane B (Zhang et al., 2013b) was fabricated of different module lengths, the module length was inversely proportional to the water permeate flux. This is because of the higher feed temperature drop along the longer fibers. Long fibers exhibit high heat transfer areas that lead to higher heat transfer rates, which in turn reduce the solution vapor pressure with its temperature reduction, thus deceasing the driving force of the mass transfer across the fiber wall.

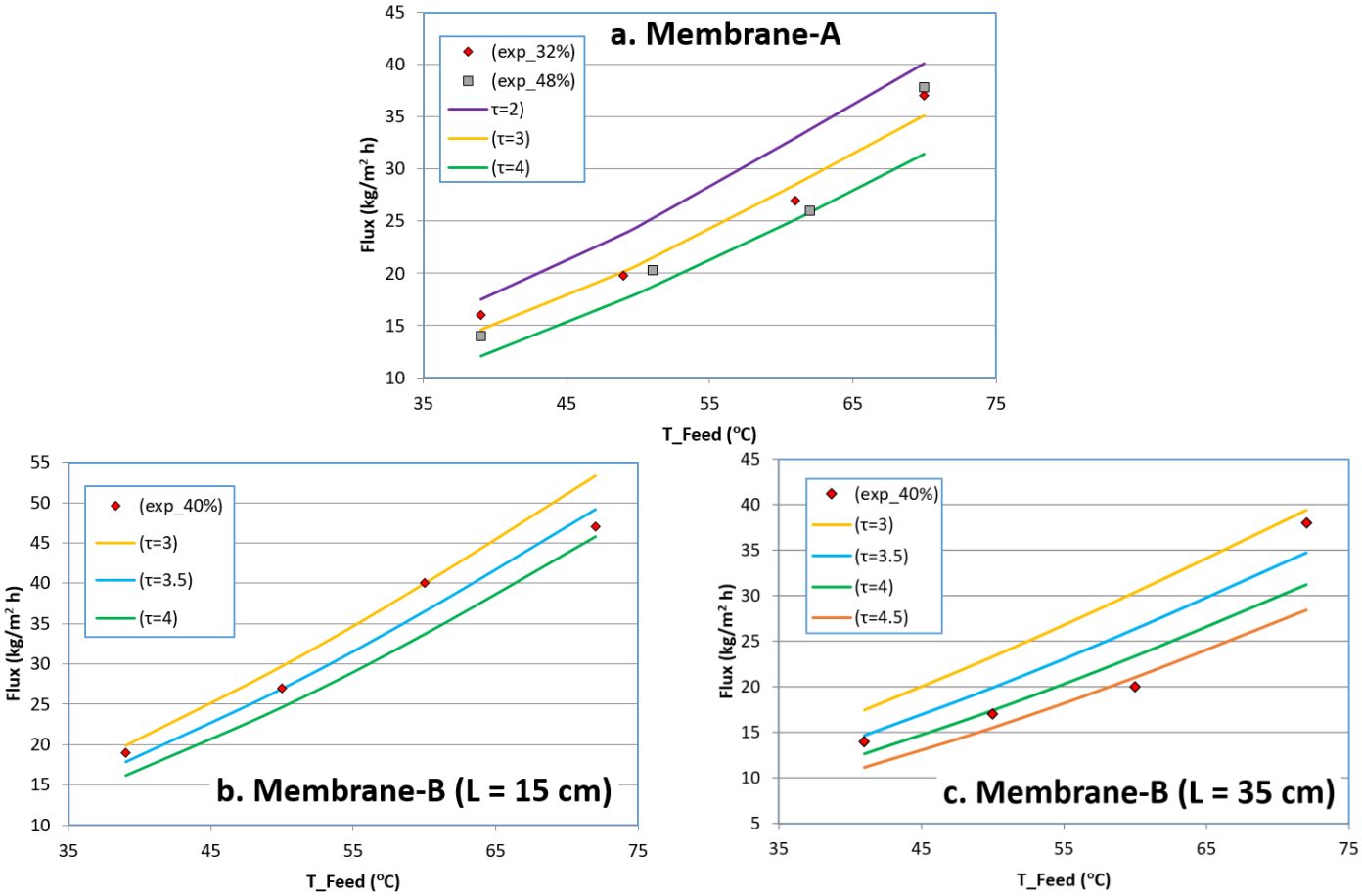

Figure 6. Effect of inlet feed temperature on permeate flux experimentally [42] and theoretically. [u_F = 0.81 m/s, P^{vacm} = 3 kPa_abs and salinity = 120 µS/cm].

Moreover, from Figures 6b and c, it can be seen that the higher tortuosity more appropriately predicted the flux for the longer module than for the shorter one. This may confirm the temperature effect on the membrane characteristics during the VMD operation, where the average temperature was lower for the longer module than for the shorter one; therefore, the solution vapor pressure was higher in the shorter module. Zhang et al. (2013b) [42] reported that the value of the tortuosity of membrane A was about twice that of membrane B, but this was not observed in the present study. Also, Zhang et al. (2013b) [42] reported from the experimental work that there was a permeate flux decay of more than 25% observed for membrane B at various feed velocities and at a constant temperature and vacuum pressure when they repeated the experiments. For membrane A with four experiments and two repeats of each experiment, the flux did not vary considerably between the two analyses, although there was a decline in the flux during the experimental operation after about 250 min. Zhang et al. (2013b) [42] reported that membrane A regained its initial permeation flux at rest, whereas membrane B was not able to regain its initial permeation flux. This may be due to the structure of the membrane, and they suggested that more research is needed to understand this phenomenon. Comparing the results predicted by both the developed model and the

experimental work demonstrated that the wide distribution of the pore size of the fiber could be one of the main reasons for the deviation between the simulated and experimental results.

Effect of the permeate pressure

The permeate (vacuum) pressure is an essential parameter that greatly affects the permeate flux in VMD by making it higher than with other configurations of MD. The total pressure gradient at the two fiber sides caused convective mass flow within the pores to contribute to the total mass transfer of VMD. This feature is unique to VMD; in other MD configurations, the mass transfer only occurs by the diffusive flux of more volatile compounds through the pores of the fiber due to constant total pressure across the membrane. According to Eq. 11, the permeate flux in the VMD process increases linearly with increases in the vacuum degree in the permeate zone if the membrane characteristics are constant during the operation, with various permeate vacuum pressures. However, as mentioned above, some studies found that the characteristics of the fiber might have varied progressively throughout the MD experimental operation because of fiber compression under the high pressure gradient [38, 39, 42].

Figure 7 depicts the influence of the permeate vacuum pressure for the VMD process in Table 2 on the permeate mass flux for both the experimental data of [19] and the results of developed model. From Figure 7, it is clear that there is a sharp decay in the experimental permeate flux with a high absolute pressure (low vacuum degree) at the permeate side. However, in the simulation, a higher value of tortuosity (low MDC) was required at a higher absolute pressure to obtain a reasonable fit with the experimental results. The permeate flux results for the developed model were also compared with the experimental data of different modules reported by [44], which are summarized in Table 2 and shown in Figure 8. This data also presents a sharper decay in the permeate flux of the experimental data than in the simulation results, with increases in the absolute pressure at the permeate zone. Therefore, to provide agreement between the experimental and predicted model results required a higher resistance in the theoretical model to mass transfer at a higher absolute pressure on the permeate side (i.e., a lower mass-transfer coefficient or MDC). This was needed because the slope of the approximately linear relation of the experimental permeate flux with pressure was smaller than that of the simulation results. Additionally, the simulation results exhibited a linear relation for all values of the tortuosity.

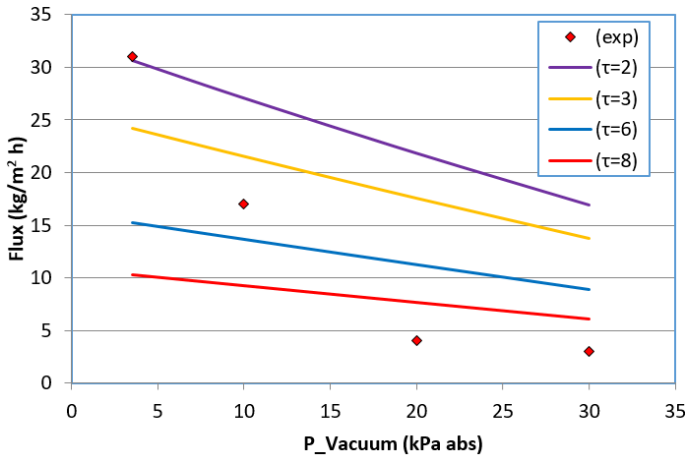

Figure 7. Effect of permeate vacuum pressure on permeate flux experimentally [19] and theoretically. [T_F = 60˚C, u_F = 0.81 m/s, and salinity = 120 µS/cm].

According to Eq. 11, the permeate flux depends on the MDC (K_i^M) and pressure difference at the two membrane sides (ΔP), and it can be expressed as $N_i = K_i^M \Delta P$. The pressure difference (ΔP) depends upon the feed temperature, permeate vacuum pressure, and feed concentration. Thus, at a constant feed temperature and concentration, the vacuum pressure is the governing parameter of the permeate flux, according to Eq. 11. Moreover, the MDC (K_i^M) is also affected by the permeate pressure, as mentioned above because it reduces the mean pore size and porosity due to membrane compression. To obtain the best agreement between the simulation and the experimental results, higher tortuosity values were required (see Figure 8) due to a higher change required for K_i^M along with the permeate pressure change. Therefore, this sharp decay in the experimental permeate flux with a change in pressure indicated a significant modification in the membrane characteristics, confirming the effect of the membrane compressibility combined with the pressure difference (ΔP) found by [38, 39, 42]. For the membrane P-220, a higher value of tortuosity was required at higher absolute permeate pressure for good agreement between the predicted and experimental data, as shown in Figure 8d. Therefore, this membrane was selected to show the effect of other membrane characteristic changes in terms of porosity and pore size, as shown in Figure 8e. In this figure, it is clear that the mean pore size and porosity had a significant effect on the simulation results. By assuming a reduction in the mean pore size from 0.46 µm to 0.2 µm and in the porosity from 0.634 to 0.5, a good fitting of the developed model's results with the experimental data was observed when using a reasonable tortuosity values.

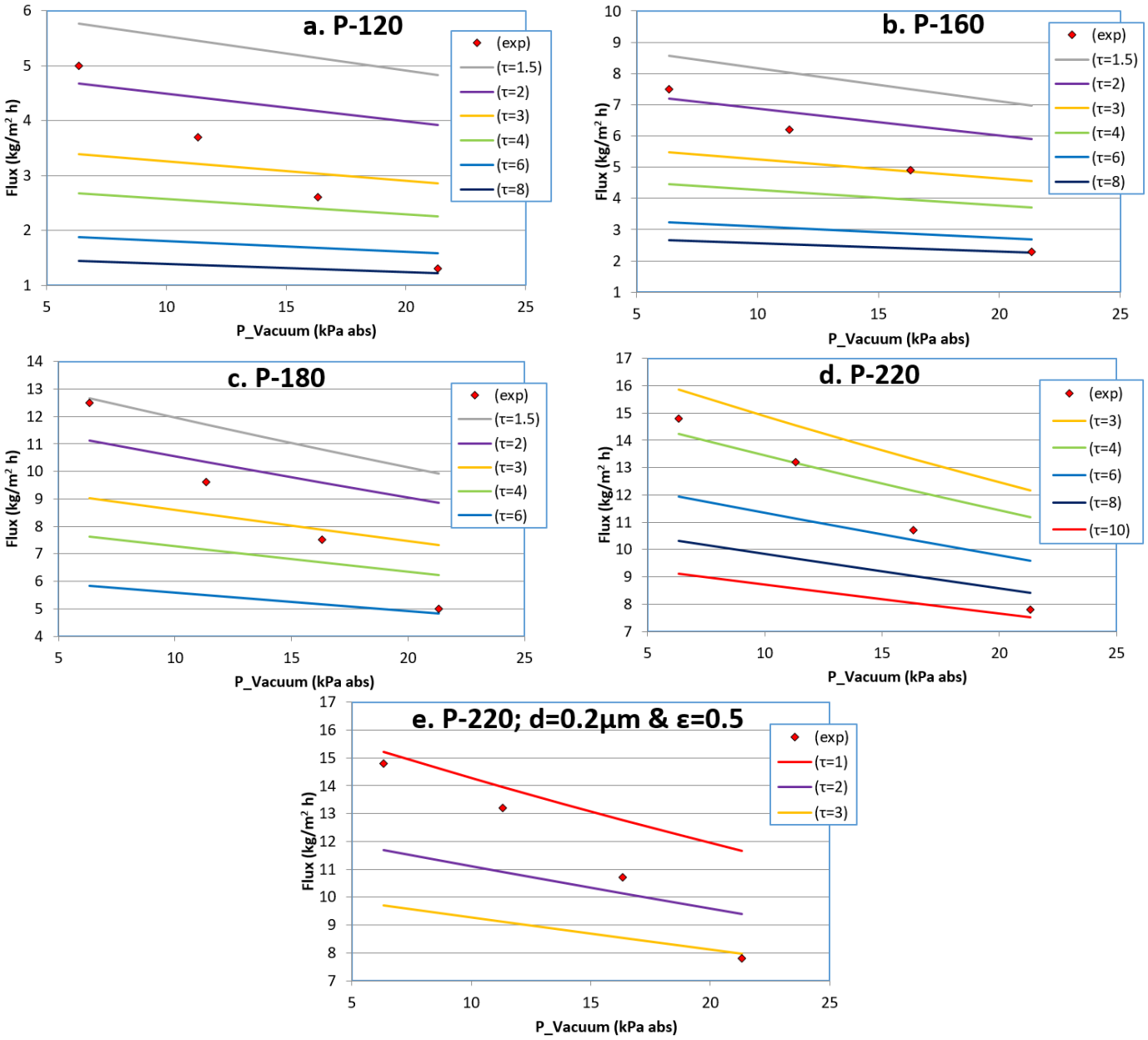

Figure 8. Effect of permeate vacuum pressure on permeate flux experimentally [44] and theoretically. [T_F = 70˚C, Q_F = 40 l/h, and salt concentration = 3 wt%].

These results strongly indicate that a change occurred in the membrane characteristics during the VMD operation. Moreover, when the absolute permeate pressure increased (i.e., the degree of vacuum decreased), the conduction heat losses by the membrane matrix increased. Therefore, the evaporation decreased because of the contribution of conduction to the water evaporation in the heat transfer within the fiber, which reduced the permeate flux.

Effect of the salt concentration

Generally, in the MD process, the permeate flux decreases with increasing salt concentrations in the feed stream due to the direct effect of the salt concentration on the activity coefficient of water. Also, the salt concentration causes the boiling point of salty solutions to rise, so the vapor pressure of these solutions decreases because of the effect of

intermolecular interaction (attraction force) between the ions molecules of the dissolved salt and the polar water molecules. The liquid water molecules need more molecular kinetic energy to be released from the effect of intermolecular interaction and to transform into the vapor phase. Therefore, the vapor pressure decreases. For example, the vapor pressure of seawater is approximately 0.18 bar at 60°C, while it is 0.2 bar for pure water at the same temperature. The MD process provides significantly fewer effects of the feed concentration on the permeate flux than that of other pressure-driven membrane separation processes used for desalination. For example, the permeate flux declined by about 30% at a constant feed temperature, vacuum pressure, and flow rate for the VMD process operated at feed NaCl concentrations of 10-100 g/L, with very high salt rejections (i.e., 99.9%), as reported by [44]. Also, a wide range of salt concentrations of saline water could easily be treated using the MD process, with a lower operating cost than other pressure-driven membrane processes.

Figure 9 depicts the impact of the inlet feed concentration (i.e., constant feed flow rate and temperature) on the permeate flux using the experimental data from [44] and the theoretical results of the developed model. In all membranes, the permeate flux decreased when the concentration of the inlet feed increased. However, Figure 9 shows that there is a difference between the theoretical and experimental results in the rate of the permeate flux drop with increased salt concentration. The effect of the vapor pressure and water activity coefficient were not significant on the permeate flux within the studied limit of salt concentrations. At a constant temperature, the vapor pressure decreased by less than 10% with a change in the salt concentration of 10-100 g/l (i.e., 1-10 wt.%) of the NaCl solution, as shown in Figure 10. Figure 10 is based on Chou's (1968) [35] equations of the vapor pressure ratio of the NaCl solution to pure water with the NaCl concentration (weight% and mole%) at various temperatures of the MD operational range. Also, the change in the water activity coefficient was less than 4% for pure water at the same NaCl concentration range of 10-100 g/l, as shown in Figure 11. Figure 11 is based on Eq. 11b of the water activity coefficient of the NaCl solution, using the weight and mole percent of the NaCl solution. Therefore, the simulation results have shown less impact of the NaCl concentration at the feed side on the water partial pressure than the higher decay of the experimental permeation flux. The higher inlet feed salt concentration led to a higher salt concentration at the fiber feed faced surface, which may reduce the porosity and pore size because the accumulation of these salt molecules might obstruct the vapor transport across the fiber.

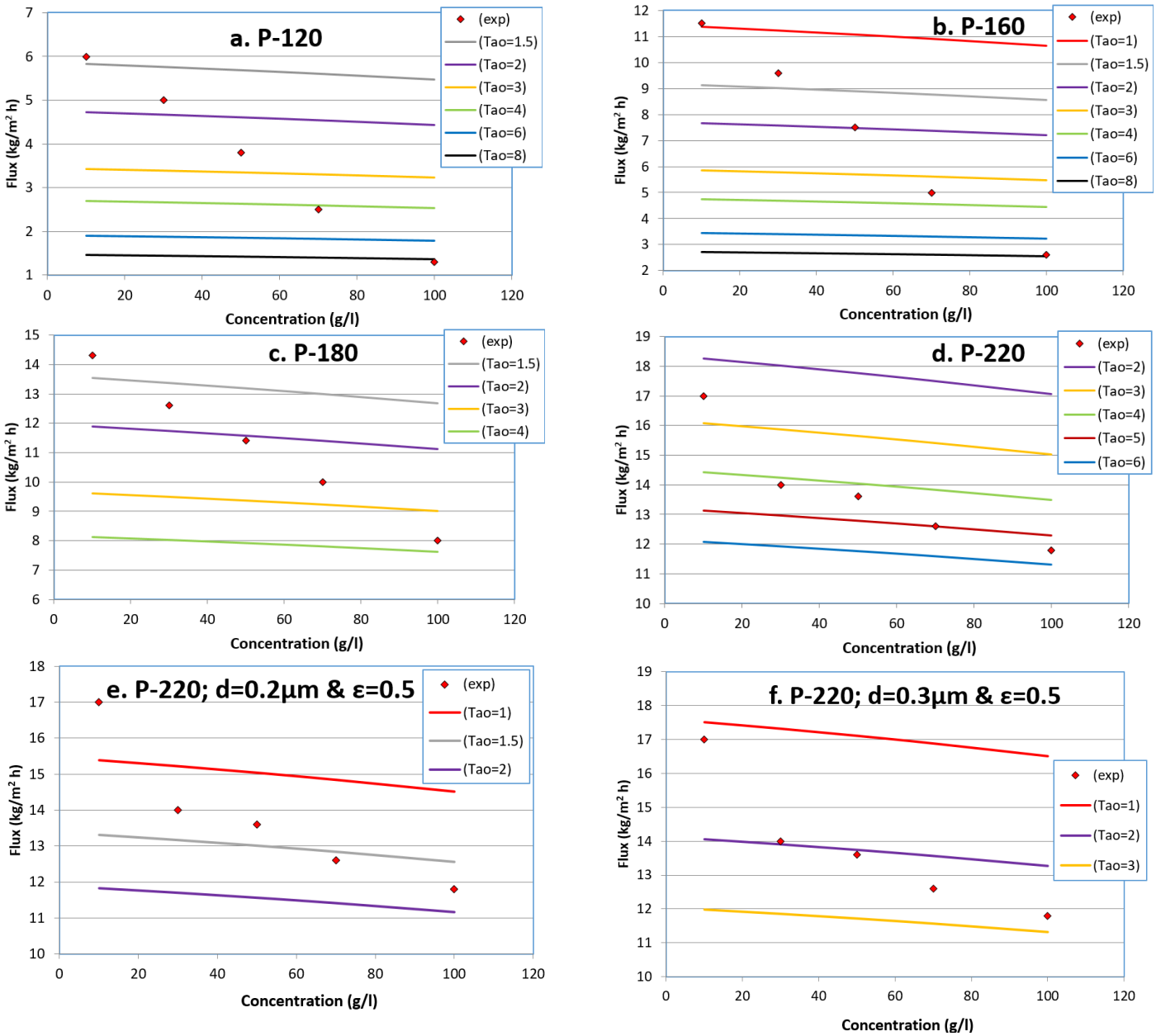

Figure 9. Effect of feed concentration on permeate flux experimentally [44] and theoretically. [T_F = 70˚C, Q_F = 40 l/h, and P^{vacm} = 6.325 kPa_abs].

This means that there is an extra resistance to the mass transfer build-up against the water movement across the membrane. Moreover, Zhu et al. (2013) [44] reported increases in the electrical conductivity of the permeate flux and decreases in the salt rejection percent as the salt concentration of the feed solution increased. In fact, a slight degree of membrane wetting occurred; however, the salt rejection was high (about 99.9%) at the maximum salt concertation of 100g/l. Increases in the permeate conductivity can be attributed to the slight decrease in the liquid entry pressure (LEP) with the increasing salt concentration due to a slight decrease in the surface tension of the solution, according to the Laplace (Cantor) equation of the LEP:

$$LEP = -\frac{2B\gamma_{sol}}{r_{max}} Cos\theta \qquad (14)$$

where B is a geometric factor, γ_{sol} is the solution surface tension, θ is the membrane contact angle, and r_{max} is the maximum membrane pore size.

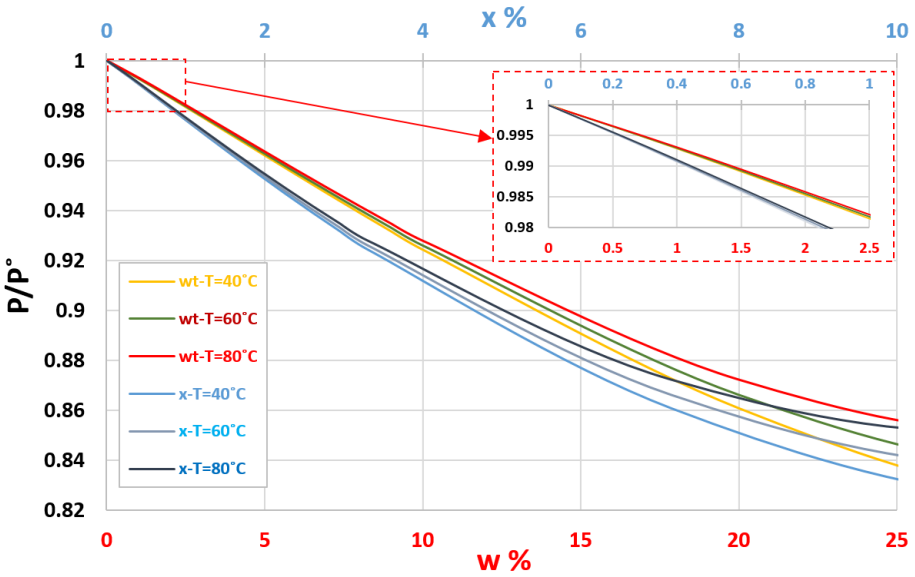

Figure 10. Vapor pressure ratio of NaCl Solution to pure water with weight percent and mole percent of NaCl solutions at various temperatures.

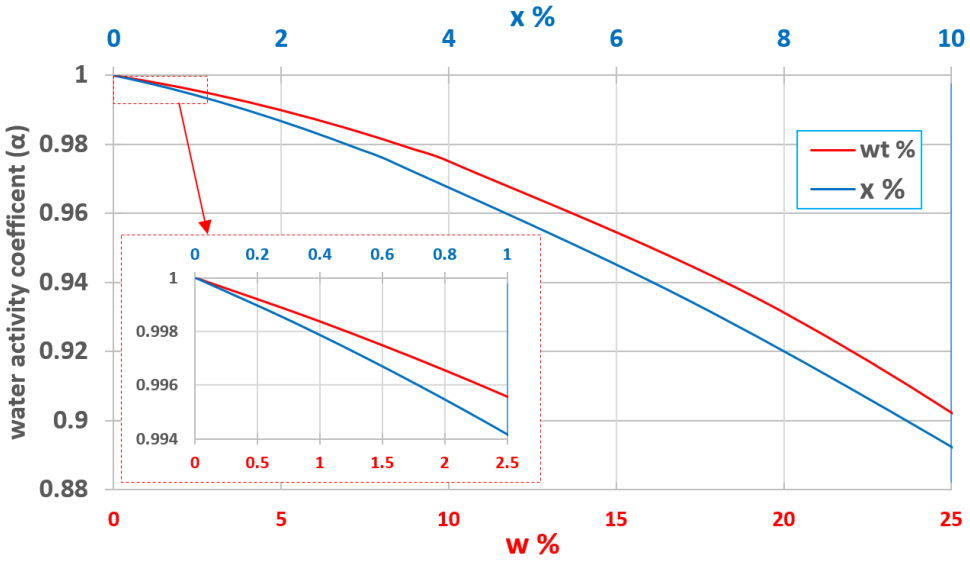

Figure 11. Water activity coefficient with weight percent and mole percent of NaCl salt concentrations according to Eqn. (11b).

Figures 9 e and f demonstrate the significant influence of fiber characteristics (i.e., porosity, pore size, and tortuosity) for the membrane P-220 when adjusting the simulation results to fit the experimental results. In Figure 9e, the simulation results assumed a reduction in the mean pore size from 0.46 μm to 0.2 μm and in the porosity from 0.634 to 0.5, whereas Figure 9f displays a reduction in the mean pore size from 0.46 μm to 0.3 μm and in the porosity from 0.634 to 0.5. In Figures 9 e and f, there are significant effects of the pore size and porosity of

the feed face membrane change during the VMD operation at a high feed concentration. However, Figure 9 depicts a higher effect of the salt concentration on the permeate flux drop in the VMD configuration than that reported for DCMD. In Figure 9, when the salt concentration increased into the range from 1-10 g/l, the permeate flux significantly decayed by about 78, 77, 44, and 30% for the membranes P-120, P-160, P-180, and P-220, respectively. Other research, such as [45], reported that the decay in the flux when the concentration increased into the range from 0.5-1.3 M of NaCl solution was about 33, 22, and 7.4%, respectively, at temperatures of 50, 60, and 70°C for the VMD process using the flat sheet module. Also, Safavi and Mohammadi (2009) [46] reported that the flux decayed by 23 and 36%, respectively, at 15 and 30 ml/s feed flow rates when the concentration increased between 100-300 g/l of the NaCl solution for the VMD process with a flat sheet module. Mericq et. al. (2010) [47] reported that there was a 19% drop in the permeate flux when the NaCl concentration in feed solution ranged from 50 to 300 g/l for the VMD process using a flat sheet module. The concentration effect in the VMD process was higher than in the DCMD process, with [43] indicating that when the concentration of NaCl in the feed stream increased from 0 to 2 M, the flux decreased by about 12%.

Effects of the feed flow rate

In the VMD process, increasing the feed flow rate (i.e., increasing the Reynolds number) also played a significant role in enhancing the permeate flux by decreasing the boundary layer resistance adjacent to the fiber surface at the feed side. Thus, the temperature and concentration differences between the bulk and fiber surfaces at the feed side will decrease, which in turn reduces the effects of the temperature and concentration polarization. Moreover, increasing the feed velocity reduces the residence time of the hot feed in the module. Therefore, the temperature drops in the feed stream decreases, causing the average temperature of the feed with its corresponding solution vapor pressure to increase.

The MDC (K_i^M) in Eq. 11 changes very slightly with the feed velocity unless there are significant changes in the membrane characteristics. The permeate flux variation with various feed velocities is largely due to the reduced temperature polarization resistance. This permeate flux variation decreases the boundary layer thickness of the heat and mass transport and also increases the feed vapor pressure as the average bulk feed temperature increases at higher velocities. However, Zhang et al. (2013b) [42] indicated that compared with the DCMD process, the thickness of the boundary layer had little effect on this flux in the VMD process.

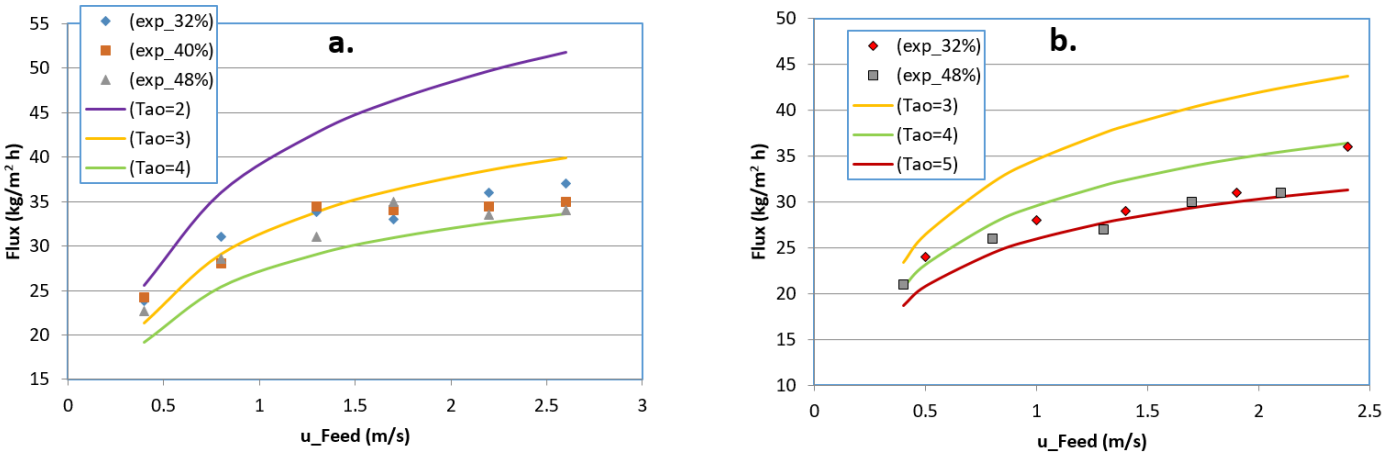

Figure 12. Effect of feed inlet velocity on permeate flux experimentally and theoretically. [T_F = 60˚C and salinity = 120 µS/cm] **a.** P^{vacm} = 2 kPa_abs [19] **b**. P^{vacm} = 3 kPa_abs [42].

Figures 12 a and b represent the influence of the feed flow rate on the permeate flux of the fibers experimentally using the data [19, 42] in comparison with the predicted results of the present model. Figures 12 a and b show that increasing the feed flow rate caused the experimental and theoretical permeate flux to increase. Also, the permeate flux in Figure 12a was higher than that in Figure 12b with the same change in the velocity due to the difference in the vacuum permeate pressure. Figures 12 a and b illustrate that the simulation results of the present model at different feed velocities had a relatively good agreement with the experimental results. There was better agreement between the experimental and predicted results on the influence of the feed velocity on the permeate flux than the agreement on the effect of the feed temperature, concentration, and permeate vacuum pressure. This phenomenon may have occurred because there was no significant change in the membrane characteristics with increases in the feed flow rate other than the effect of the operating pressure and temperature on these characteristics; that maybe have occurred due to the high value of the tortuosity needed for the simulation results to fit better with their corresponding experimental data, as shown in Figures 12 a and b.

However, to fit the simulation results with the corresponding experimental results, a higher tortuosity (lower MDC) was required to predict a more appropriate permeate flux (see Figure 12b) compared with that in Figure 12a. This is might be due to the effect of the change in the membrane characteristics as a result of the permeate pressure difference between the two cases in Figures 12 a and b. Overall, it can be concluded that the membrane characteristics changed during the VMD operation and that the developed model was verified by the broad range of experimental data collected from the literature.

Model Verification for VMD

The validation of the mathematical model for the VMD process using hollow fiber membrane modules was verified by comparing the present simulation results with experimental data using different fiber types, characteristics, module properties, and operating conditions, which were collected from the literature and are summarized in Table 2. The simulation results using the developed model to predict the VMD permeation flux were compared with a wide range of experimental work from 135 experimental data points. These data represent the variation of the water permeate flux within the main affected parameters of VMD processes. Figure 13 illustrates the present mathematical model with its simulated results compared to all of these experimental data, showing that the verification of the developed model with the experimental data from the literature is good, with acceptable accuracy.

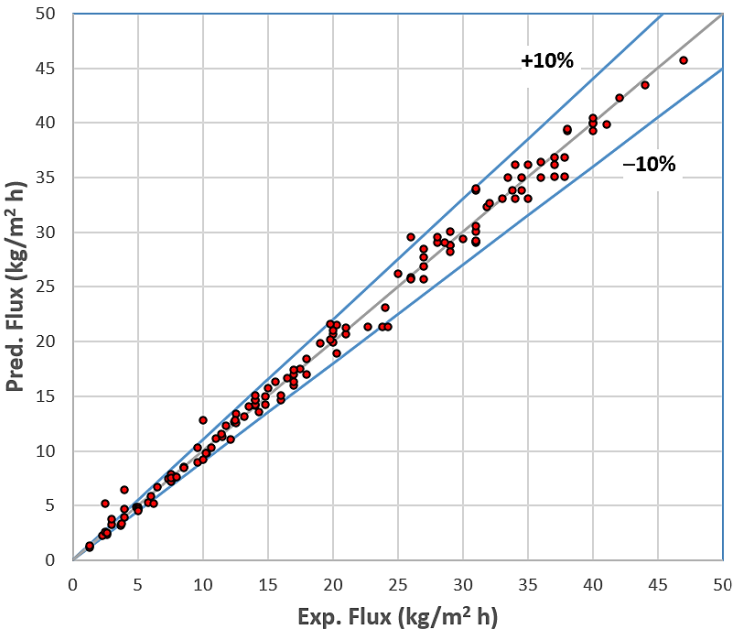

Figure 13. Comparison between the simulation results with all experimental data that haven extracted from literature for VMD process using hollow fiber module.

Conclusions

A mathematical model of simultaneous heat and mass transfer was presented to describe for the first time the changing effect of the characteristic parameters of the membrane during the VMD process of water desalination on the permeation flux in a shell-and-fibers module. The developed model was based on the numerical solving of the simultaneous energy and mass balances governing equations for the hollow fiber VMD process used for water desalination using the MATLAB® software program. The present developed model took into account the major concepts of the desalination process via VMD in terms of the affected parameters related to membrane characteristics, operating conditions,

and module properties. This model considered a combination of Knudsen diffusion and viscous flow mechanisms for water vapor mass transfer across the membrane. The conductive heat transfer within the membrane was neglected due to the applied vacuum pressure at the permeate zone. The performance of the present developed model was tested by comparing its prediction of permeate flux with a wide range of experiments (i.e, 135 experimental points) obtained from the literature. The experiments described the influence of the operating conditions (i.e., feed temperature, concentration, velocity, and permeate vacuum pressure), module design (i.e., packing density and module length), and membrane characteristics (i.e., types, pore size, porosity, thickness, and tortuosity) on the permeate flux of pure water. This study concluded that there is a high likelihood of obtaining changes in the membrane characteristics during the VMD process, which also confirmed the conclusions presented in some of the previously published experimental studies. Membrane characteristics have a significant effect on the permeate flux. The assumed tortuosity value was used to explore how membrane characteristics changed during operation by using the tortuosity value as a tuning parameter to upgrade the performance of the model. The validity of the present model was tested in terms of the permeate flux prediction, and a good agreement was obtained between the simulation results of the present model and the experimental data from the literature.

Nomenclatures

Capital letters

A	Surface area (m^2)
B	Geometric factor
C	Concentration ($gmol/m^3$)
D	Hollow fiber diameter (m)
D_{AB}	Diffusivity (m^2/s)
H	Enthalpy (kJ/kg)
K	Membrane distillation coefficient ($kg/Pa.m^2.s$)
L	Effective membrane length (m)
LEP	Liquid entrance pressure (Pa)
Mwt	Molecular weight (g/gmol)
N	Permeate mass flux ($kg/m^2.s$)
Q	Heat transfer rate (W)
P^V	Vapor pressure (Pa)
$\bar{P}$	Average pressure (Pa)
R	Universal gas constant (8.314 J/gmol.K)
T	Temperature (˚C or K)

Greek letters

ΔH	Latent heat of vaporization (kJ/kg)
α	Activity coefficient
β	Membrane permeability ($kg/Pa.m^2.s$)
γ	Surface tension (N/m)
δ	Membrane thickness (m)
ε	Porosity
θ	Contact angle (˚)
μ	Viscosity (Pa.s)
ρ	Density (kg/m^3)
λ	Mean molecular free path (m)
σ	Collision diameter
τ	Tortuosity

Subscripts

aq	Aqueous
B	At the bulk
i	Cells counter

$\bar{T}$	Average temperature (˚C or K)

Lower case letters

d	Pore size (diameter) (m)
h	Heat transfer coefficient (W/m^2 K)
k	Thermal conductivity (W/m.K)
k	Mass transfer coefficient (m/s) or (m/h)
k_B	Boltzmann constant (1.381× 10^{-23} J/K)
l	Cell length (m)
m	Mass flow rate (kg/s)
p	Partial pressure (Pa)
r	Pore radius (m)
ri	Internal hollow fiber radius (m)
w	Weight fraction
x	Mole fraction

M	Membrane surface
ro	Based on external radius
ri	Based on internal radius
s	Solid
T	Total
w	Water

Superscript

F	Feed side
K	Knudson diffusion
L	Liquid
M	Membrane
P	Permeate side
V	Viscous flow
F	Feed side

References

1. Li, Y., Tian, K., 2009. Application of vacuum membrane distillation in water treatment. J. Sustainable Development 2, 183-186.
2. Sridhar, S., Moulik, S., 2019. Membrane Processes: Pervaporation, Vapor Permeation and Membrane Distillation for Industrial Scale Separations. John Wiley & Sons, Scrivener Publishing LLC.
3. Greenlee, L. F., Lawler, D. F., Freeman, B. D., Marrot, B., 2009. Reverse osmosis desalination: Water sources, technology, and today's challenges. Water Research 43, 2317-2348.
4. Mohammadi, T., Safavi, M. A., 2009. Application of Taguchi method in optimization of desalination by vacuum membrane distillation. Desalination 249, 83–89.
5. Pangarkar, B. L., M.G. Sane, Parjane, S. B., Guddad M., 2011. Vacuum Membrane Distillation for Desalination of Ground Water by using Flat Sheet Membrane. Int. J. Chem. Biomol. Eng. 4, 13-18.
6. Khayet, M., and Matsuura, T. T., 2011. Membrane Distillation Principles and Applications. Oxford- UK. Elsevier.
7. Khalifa, A. E., 2015. Water and air gap membrane distillation for water desalination – An experimental comparative study. Sep. Purif. Tech. 141, 276–284.
8. Chiam, C., Sarbatly R., 2013. Vacuum membrane distillation processes for aqueous solution treatment—A review. Chemical Engineering and Processing 74, 27– 54.

9. Olatunji, S. O., Camacho L. M., 2018. Heat and Mass Transport in Modeling Membrane Distillation Configurations: A Review, Front. Energy Res., 6:130, 1-19.
10. Sivakumar, M., Ramezanianpour, M., O'Halloran, G., 2013. Mine Water Treatment Using a Vacuum Membrane Distillation System. APCBEE Procedia 5, 157 – 162.
11. Anqi, A. E., Usta, M., Krysko R., Lee, J., Ghaffour N., Oztekin A., 2020. Numerical study of desalination by vacuum membrane distillation–Transient three-dimensional analysis. J. Membr. Sci. 596, 117609.
12. Bandini, S., Saavedra, A., Sarti, G.C., 1997. Vacuum membrane distillation: Experiments and modeling. AIChEJ. 43, 398–408.
13. Bandini, S., Sarti, G.C., 1999. Heat and mass transport resistances in vacuum membrane distillation per drop. AIChE J. 45, 1422–1433.
14. Banat, F., Al-Rub, F.A., Bani-Melhem, K., 2003. Desalination by vacuum membrane distillation: Sensitivity analysis. Sep. Purif. Technol. 33, 75–87.
15. Mengual, J.I., Khayet, M., Godino, M.P., 2004. Heat and mass transfer in vacuum membrane distillation. Int. J. Heat Mass Transfer 47, 865–875.
16. Xu, Z., Pan, Y., Yu, Y., 2009. CFD simulation on membrane distillation of NaCl solution. Front. Chem. Eng. Chin. 3, 293–297.
17. Pangarkar, B.L., Parjane, S.B., Abhang, R.M., Guddad, M., 2010. The heat and mass transfer phenomena in vacuum membrane distillation for desalination, Int. J. Chem. Biomol. Eng. 3, 33–38.
18. Fan, H., Peng, Y., 2012. Application of PVDF membranes in desalination and comparison of the VMD and DCMD processes. Chemical Engineering Science 79, 94–102.
19. Zhang, J., Li, J., Duke, M., Hoang, M., Xie, Z., Groth, A., Tun, C., Gray, S., 2013a. Modelling of vacuum membrane distillation. J. Membr. Sci. 434, 1–9.
20. Cao, W., Mujtaba, I. M., 2015. Simulation of Vacuum Membrane Distillation Process for Desalination with Aspen Plus. Ind. Eng. Chem. Res., 54, 672-680.
21. Upadhyaya, S., Singh, K., Chaurasia, S.P., Dohare, R. K., Agarwal, M., 2016a., Mathematical and CFD modeling of vacuum membrane distillation for desalination. Desalination and Water Treatment, 57, 11956-11971.
22. Upadhyaya, S., Singh, K., Chaurasia, S.P., Dohare, R. K., Agarwal, M., 2016b. Agarwal, Recovery and development of correlations for heat and mass transfer in vacuum membrane distillation for desalination.Desalination and Water Treatment 55, 26886-26898.
23. Li, L. and Sirkar, K. K., 2017. Studies in vacuum membrane distillation with flat membranes, J. Membr. Sci. 523, 225–234.
24. Kim, Y. D., Kim, Y. B., Woo, S. Y., 2018. Detailed modeling and simulation of an out-in configuration vacuum membrane distillation process. Water Research 132, 23-33.
25. Karanasiou A., Kostoglou, M., Karabelas A., 2018. An Experimental and Theoretical Study on Separations by Vacuum Membrane Distillation Employing Hollow-Fiber Modules. Water 10, 947-963.
26. Zrelli, A., Chaouachi B., 2019. Modeling and simulation of a vacuum membrane distillation plant coupled with solar energy and using helical hollow fibers. Brazilian Journal of Chemical Engineering 36, 1119 – 1129.
27. Lawson, K.W. and Lloyd, D.R., 1997. Membrane distillation, J. Membr. Sci. 124, 1–25.
28. Cao, W., Liu, Q., Wang, Y., Mujtaba, I.M., 2016 Modeling and simulation of VMD desalination process by ANN. Computers and Chemical Engineering 84, 96-103.

29. Yang, C., Peng, X., Zhao, Y., Wang, X., Fu, J., Liu, K., Li, Y., Li, P., 2020. Prediction model to analyze the performance of VMD desalination process. Computers and Chemical Engineering 132, 106-619.
30. Wang, C., 2011. On the heat transfer correlation for membrane distillation. Energy Conversion and Management 52, 1968–1973.
31. Ibrahim, S. S., Alsalhy, Q. F., 2013. Modeling and Simulation for Direct Contact Membrane Distillation in Hollow Fiber Modules. AIChEJ. 59, 589-603.
32. Andrjesdóttir, Ó., Ong, C. L., Nabavi, M., Paredes, S., Khalil, S. G., Poulikakos, D. A., 2013. An experimentally optimized model for heat and mass transfer in direct contact membrane distillation. Int. Heat J. Mass Trans. 66, 855–867.
33. Hitsov, I., Maere, T., De Sitter, K., Dotremont, C., Nopens I., 2015. Modelling approaches in membrane distillation: A critical review. Separation and Purification Technology 142, 48‑64.
34. Bui, VA, Vu, L.T.T., Nguyen, M. H., 2010. Modelling the simultaneous heat and mass transfer of direct contact membrane distillation in hollow fiber modules. J. Membr. Sci. 353, 85-93.
35. Chou, J. C., 1968. Thermodynamic properties of aqueous sodium chloride solutions from 32 to 350˚F. PhD thesis. Oklahoma State University.
36. Hayer, H., Bakhtiari, O., Mohammadi, T., 2015. Analysis of heat and mass transfer in vacuum membrane distillation for water desalination using computational fluid dynamics (CFD). Desalination and Water Treatment 55, 39-52.
37. Alsalhy, Q. F., Ibrahim, S. S., Hashim, F. A., 2018. Experimental and theoretical investigation of air-gap membrane distillation process for water desalination. Chemical Engineering Research and Design 130, 95–108.
38. Zhang, J., Li, J., Gray, S., 2011. Effect of applied pressure on performance of PTFE membrane in DCMD. J. Membr. Sci. 369, 514–525.
39. Zhang, J., Gray, S., Li, J., 2012. Modelling heat and mass transfers in DCMD using compressible membranes, J. Membr. Sci. 387–388, 7–16.
40. Eykens, L., Sitter, K. D., Dotremont, C., Pinoy, L., Bruggen B. V., 2016. How to optimize the membrane properties for membrane distillation: A Review. Ind. Eng. Chem. Res. 55, 9333-9343.
41. Jeong, S., Lee, S., Chonc, H., and Seockheon Lee., 2014. Structural analysis and modeling of the commercial high performance composite flat sheet membranes for membrane distillation application. Desalination 349, 115-125.
42. Zhang, J., Li, J., Duke, M., Hoang, M., Xie, Z., Groth, A., Tun, C., Gray, S., 2013b. Influence of module design and membrane compressibility on VMD performance. J. Membr. Sci. 442, 31–38.
43. Qtaishat, M., Matsuura, T., Kruczek, B., Khayet, M., 2008. Heat and mass transfer analysis in direct contact membrane distillation, Desalination 219, 272-292.
44. Zhu, H., Wang, H., Wang, F., Guo, Y., Zhang, H., Chen, J., 2013. Preparation and properties of PTFE hollow fiber membranes for desalination through vacuum membrane distillation. J. Membr. Sci. 446, 145–153.
45. Tang, N., Cheng, P., Wang, X., Zhang, H., 2009. Study on the Vacuum Membrane Distillation Performances of PVDF Hollow Fiber Membranes for Aqueous NaCl Solution. 9th International Conference on Chemical and Process Engineering. Chemical Engineering Transactions 17, 1537-1542.
46. Safavi, M., Mohammadi, T., 2009. High-salinity water desalination using VMD. Chemical Engineering Journal 149, 191–195.
47. Mericq, J., Laborie, S., Cabassud, C., 2010. Vacuum membrane distillation of seawater reverse osmosis brines. water research 44, 5260-5273.